Interfacial Morphology Addresses Performance of Perovskite Solar Cells Based on Composite Hole Transporting Materials of Functionalized Reduced Graphene Oxide and

**Article type:** Full Paper

# Interfacial morphology addresses performance of perovskite solar cells based on composite hole transporting materials of functionalized reduced graphene oxide and P3HT

Teresa Gatti*, Francesco Lamberti, Peter Topolovsek, Mustapha Abdu-Aguye, Roberto Sorrentino, Luca Perino, Marco Salerno, Leonardo Girardi, Carla Marega, Gian Andrea Rizzi, Maria Antonietta Loi, Annamaria Petrozza and Enzo Menna*.

Dr. T. Gatti, Dr. F. Lamberti, L. Perino, L. Girardi, Prof. C. Marega, Prof. G. A. Rizzi, Prof. E. Menna
Department of Chemical Sciences, University of Padova, Via Marzolo 1, 35131 Padova, Italy
E-mail: teresa.gatti@unipd.it; enzo.menna@unipd.it
Dr. T. Gatti, Prof. C. Marega, Prof. G. A. Rizzi, Prof. E. Menna
INSTM UdR Padova, Via Marzolo 1, 35131 Padova, Italy
Dr. F. Lamberti, Prof. G. A. Rizzi, Prof. E. Menna
Interdepartmental Centre "Giorgio Levi Cases" for Energy Economics and Technology, University of Padova, Via Marzolo 9, 35131 Padova, Italy
Dr. P. Topolovsek, R. Sorrentino, Dr. A. Petrozza
Center for Nanoscience and Technology, Istituto Italiano di Tecnologia, Via Pascoli 70/3, 20133 Milano, Italy
M.Abdu-Aguye, Prof. M. A. Loi
Photophysics and OptoElectronics, Zernike Institute of Advanced Materials, Rijksuniversiteit Groningen, Nijenborgh 4 NL-9747 AG, Groningen, The Netherlands
Dr. M. Salerno
Materials Characterization Facility, Istituto Italiano di Tecnologia, Via Morego 30, 16163 Genova, Italy

**Keywords.** Perovskite solar cells, reduced graphene oxide, composites, hole transporting materials, interfacial engineering

**Abstract**

The development of novel hole transporting materials (HTMs) for perovskite solar cells (PSCs) that can enhance device's reproducibility is a largely pursued goal, even to the detriment of a very high efficiency, since it paves the way to an effective industrialization of this technology. In this work we study the covalent functionalization of reduced graphene oxide (RGO) flakes with different organic

functional groups with the aim of increasing the stability and homogeneity of their dispersion within a poly(3-hexylthiophene) (P3HT) HTM. The selected functional groups are indeed those recalling the two characteristic moieties present in P3HT, *i.e.* the thienyl and alkyl residues. After preparation and characterization of a number of functionalized-RGO@P3HT blends, we test the two containing the highest percentage of dispersed RGO as HTMs in PSCs and compare their performance with that of pristine P3HT and of the standard Spiro-OMeTAD HTM. Results reveal the big influence of the morphology adopted by the single RGO flakes contained in the composite HTM in driving the final device performance and allow to distinguish one of these blend as a promising material for the fabrication of highly reproducible PSCs.

## 1. Introduction

A great interest is devoted to functional composite materials based on organic semiconductors and carbon nanostructures (CNSs) for optoelectronic applications.[1-5] Excluding polymer/small molecule – fullerene blends for organic photovoltaics, which constitutes a unique and wide chapter apart,[6, 7] the other most relevant cases include carbon nanotubes or graphene composites with conjugated polymers such as polythiophenes, polyfluorenes or narrow bandgap donor-acceptor polymers, for use in field effect transistors (FETs),[8-13] thermoelectrics,[14, 15] supercapacitors[16-19] and flexible/wearable electronics.[20-22]

Within the graphene-based materials (GBMs) family, reduced graphene oxide (RGO) stands out for its good electronic properties, processability, low-costs, possibility to use green-chemistry methods for its production and suitability for large-scale applications.[23-27] Composites of pristine RGO with regioregular poly(3-hexylthiophene) (P3HT), the benchmark solution-processable polythiophene species, have been employed to enhance performance in a polymer-metal oxide hybrid solar cells,[28] to produce FETs with good hole mobility,[11] to boost efficiency and stability in perovskite solar cells,[29, 30] and as active materials in field emission cathodes [31] and gas sensors.[32]

In principle, RGO and P3HT have the potential to establish π-π stacking interactions between their individual delocalized π electrons clouds,[33] which can make their composites highly stable and not subjected to phase separation. Unfortunately this does not often occur due to the stronger tendency of pristine GBMs to self-aggregate, as it happens for the majority of CNSs, compromising the homogeneity of their dispersion within a polymer matrix.[1] In this regard, resorting to chemical functionalization of pristine CNSs can be useful when the process is sufficiently controllable to avoid an excessive disruption of the native electronic structure.[1, 34-36] In the past we have applied a coupled covalent chemical functionalization/sedimentation-based separation (SBS) strategy to obtain homogeneous dispersion of RGO in a P3HT matrix.[29] The chemical functionalities selected for

binding to the RGO flakes surface were the 4-(methoxy)phenyl groups (thus leading to species named as RGO-PhOMe), introduced through a Tour-type direct arylation reaction [37] and previously demonstrated to be able to improve dispersibility of other CNSs in organic solvents and polymers.[35, 38] RGO-PhOMe@P3HT blends, enriched in the most soluble fractions of the functionalized RGO derivative thanks to the SBS process, were then employed as hole transporting materials (HTMs) in standard architecture perovskite solar cells (PSCs), providing increased efficiency and stability to the devices in comparison to the use of a bare P3HT HTM.[29] An effect of the content of the nanofillers dispersed in the P3HT blend on the final device performance was evidenced by testing HTMs with different loadings of RGO-PhOMe. The HTM with the highest nanofiller content (4 wt%) was significantly outperforming the others, suggesting a correlation between CNS wt% and PSC efficiency, likely through the improvement of the hole extraction process at the perovskite/HTM interface.[29, 39] This was indeed achieved thanks to the homogeneity of dispersion of the RGO-PhOMe species in P3HT, which allowed to build optimized selective contacts.

In the search for novel, more effective, functionalized-RGO@P3HT HTMs for PSCs, we report in this work our efforts in the functionalization of pristine RGO with organic groups other than the 4-(methoxy)phenyl ones previously employed. The aim is to investigate the effect of different substituents bound to RGO flakes on the morphology of the resulting P3HT-based thin film HTMs. These functional groups have been conceived to resemble the chemical functionalities present in the P3HT structure. They are indeed the 4-(thien-2-yl)phenyl (PhTh), the 4-(5-methylthien-2-yl)phenyl (PhMeTh) and the 4-[(2-2'-bithiophene)-5-yl]phenyl (PhBiTh) moieties, containing thienyl groups recalling the polymer backbone, and the 4-(hexyloxy)phenyl (PhOHex) and 4-[(2-ethyl)hexyloxy]phenyl (PhOEtHex) moieties, containing alkyl chains, as in the polymer side-chains (see Figure 1 for a pictorial sketch of the concept). The methyl group in the 2-methylthienylphenyl substituent and the ethyl group in 2-ethylhexyloxyphenyl one have been introduced as variations to the basic thienyl and hexyl moieties, able to confer steric hindrance to the substituent.

The resulting derivatives have been blended with P3HT applying the previously used SBS protocol,[29] providing different amounts of functionalized RGO homogeneously dispersed in the polymer solution, depending on the substituents grafted on the CNS surface. From each family of RGO derivatives, *i.e.* the thienyl-based and the alkyl-based ones, the blend with the highest wt% of functionalized-RGOs has been selected to be tested as HTMs in PSCs. Their performance has been compared to that of bare P3HT and to that of the most widely used HTM in PSC, the spiro-compound 2,20,7,70-tetrakis-(*N*,*N*-di-*p*-methoxyphenylamine)9,90-spirobifluorene (Spiro-OMeTAD).[40] Surprisingly, the obtained results evidence the key role played by the chemical nature of the organic groups covalently bound to RGO in influencing final HTM film morphology and consequently

affecting devices figures of merit and reproducibility. In particular for this last aspect, a consistent improvement with respect to Spiro-OMeTAD-based PSCs is found when employing one of the tested functionalized-RGO@P3HT composites as HTM. From this work therefore, novel fruitful insights emerge for the future optimization of functionalized-RGO@P3HT composites designed as HTMs for PSCs, which might allow to overcome the limitations related to the use of Spiro-OMeTAD, such as the high costs of production, the need for doping to increase hole mobility and electrical conductivity and the scarce stability to environmental factors.[41-43] These are indeed major concerns for effectively promoting the industrialization of this photovoltaic technology.

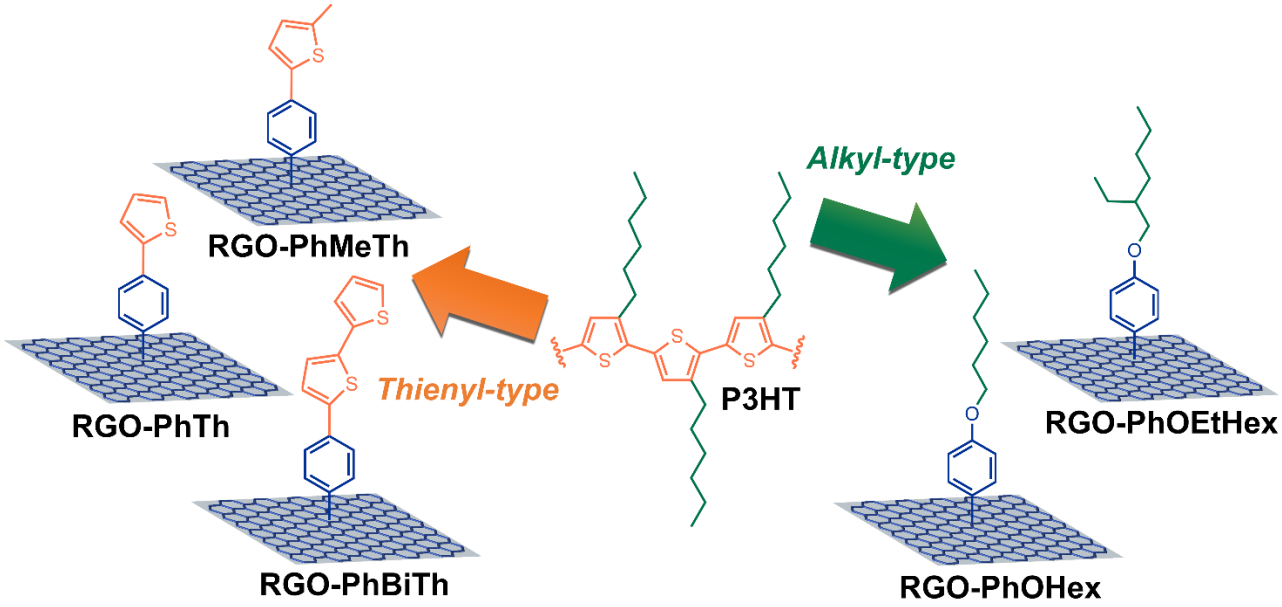


**Figure 1.** Schematic illustration of the five types of functionalized-RGO species reported in this work, highlighting the similarity relationships existing among the organic substituents covalently bound to RGO and the P3HT structure.

## 2. Results and discussion

The five types of organic moieties recalling the structure of the backbone and side chains of P3HT have been covalently bound to RGO through *in situ* direct arylation reactions, starting from the corresponding aniline derivative in the presence of isoamyl nitrite,[44] as reported in the Experimental Section (see Scheme S1 in the Supporting Information – S.I. - file for a pictorial representation of the reactions),[25, 29] furnishing the functionalized-RGO species RGO-PhOHex, RGO-PhOEtHex, RGO-PhTh, RGO-PhMeTh and RGO-PhBiTh. Details about the synthesis of the five aniline derivatives are given in the S.I. For the five different RGO functionalizations the same protocol was employed, in terms of quantity of reactants and reaction times. Due to different reactivity of the aniline precursors, the resulting functionalization degree (FD) varied among products. FDs are defined as the fraction of carbon atoms of the CNS that bear a covalently grafted functional group with respect to the total number of carbon atoms and are expressed in percentage: they can be determined with a good approximation from thermogravimetric analysis (TGA), as reported in detail in ref. [45]. FDs

extracted from TGA data for the five functionalized RGO derivatives are given in Table 1 (TGA traces are given in the S.I., Figures S1-S5). The derivative with the highest FD resulted to be RGO-PhOHex. FD couldn't be determined for RGO-PhBiTh, since the RGO backbone starts to thermally decompose when the 2,2'-bithienylphenyl moieties have not yet finished, leaving a partial superposition of the two phenomena that hinders the correct extrapolation of the data. The presence of the 2,2'-bithienylphenyl groups in the RGO derivative is anyway clearly visible from the UV-visible-NIR absorption spectrum of the functionalized-CNS dispersed in DMF, with a characteristic absorption band emerging with a maximum at 364 nm from the continuous absorption of RGO in the UV-NIR range (see Figure S6 in the S.I., where all the UV-vis-NIR spectra of the functionalized RGO derivatives are reported).

The five types of functionalized RGO materials were dispersed in P3HT following our previously reported SBS process[29] (see Experimental Section for details). In particular, starting from a suspension of functionalized-RGO/P3HT (1:10 wt/wt; *i.e.* 10 wt%) in chlorobenzene, the protocol furnishes, after discarding the insoluble residue, a final solution with a lower wt% from which composite films are then cast. In this way, the most insoluble fractions of the functionalized-RGO batch, namely those containing most of the CNS aggregates and the less chemically functionalized RGO flakes, are removed from the blend. Different final wt% contents were achieved with the different RGO derivatives. Values are reported in Table 1: as it can be observed, they all exceed the 4 wt% threshold which was previously achieved with RGO-PhOMe. This is an indication that intermolecular interactions are likely to play an active role in stabilizing the novel blend suspensions of RGO in P3HT. In addition, it is worthy to mention that, by employing pristine RGO as the filler and after applying the same protocol, only a minimal wt% of CNSs remains dispersed in the P3HT solution, further underlying the contribution of the chemical functionalization in ensuring a good quality of the dispersions,[38, 46] free from major aggregates and composed of individual RGO flakes. This is indeed a key issue for preserving most of GBMs unique properties, such as the high aspect ratio and electrical conductivity, observed with single or few layers sheets.[47] Inspection of the FD values characteristic of the insoluble residues collected after the sedimentation-based separation process reveals that these are actually the fractions of the starting functionalized-RGO materials containing the lower amounts of covalently grafted organic substituents (see Table 1), as it was expected. Interestingly, the final functionalized-RGO wt% in P3HT obtained after the SBS process is not always related to the FD of the single nanofiller. While for RGO-PhOHex a high FD corresponds to a high wt% in P3HT after SBS, the same does not apply for example to RGO-PhEtHex in comparison to RGO-PhMeTh, having the former a slightly higher FD but a significantly lower wt% in P3HT. The reasons for the lack of such a strict correlation are to be found most likely in the

different types of intermolecular interactions which are established between the polymer matrix and the substituents present on the RGO flakes. It is again evident by observing these data, that such interactions play a pivotal role in stabilizing functionalized-RGO suspensions in a polymeric medium.

**Table 1.** FDs and wt% in P3HT after the SBS process of the five different functionalized RGO derivatives reported in this work. FDs of the insoluble residues collected after the SBS process at the bottom of the centrifugation vessels.

| Functionalized RGO derivative | FD (%)[a] | wt% in P3HT[b] | FD of the insoluble residue (%)[a] |
|---|---|---|---|
| **RGO-PhOHex** | 3.2 | 6.3 | 1 |
| **RGO-PhOEtHex** | 1.6 | 5.5 | 0.8 |
| **RGO-PhTh** | 1.2 | 5.1 | 1 |
| **RGO-PhMeTh** | 1.4 | 6.2 | 0.9 |
| **RGO-PhBiTh** | NA[c] | 6.7 | NA[c] |

[a] Extracted from TGA. [b] Calculated after weighting the insoluble residues, considering an initial 10 wt% content of functionalized RGO material in P3HT before the SBS process. [c] Not available data (see main text for details).

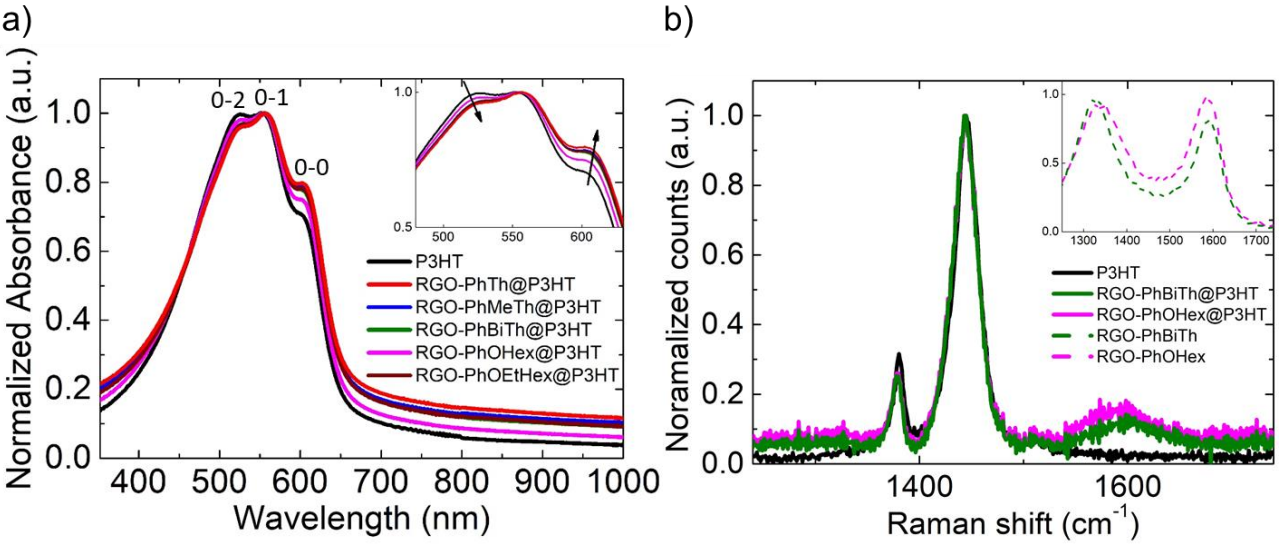


**Figure 2.** a) UV-visible-NIR absorption spectra of spin-coated thin films of P3HT and of the five types of functionalized-RGO@P3HT blends presented in this work on glass slides. The inset show a detail of the intensity variations occurring in the three P3HT vibronic transitions upon blending with functionalized-RGOs. b) Raman spectra of spin-coated thin films of P3HT and of the two functionalized-RGO@P3HT blends containing the highest wt% of dispersed CNSs. Raman spectra of the two corresponding functionalized-RGO are reported in the inset for the sake of clarity.

The optical properties of the functionalized-RGO@P3HT blends in the form of spin-coated thin films on glass substrates were characterized through UV-visible-NIR absorption spectroscopy and compared to those of bare P3HT (spectra reported in Figure 2a). The spectrum of the pure polymer shows the distinctive absorption band, characterized by three vibronic features at 526, 551 and 600 nm respectively, originated by $\pi$-$\pi^*$ electronic transitions coupled to lattice vibrations in P3HT crystalline domains.[48] In particular, the 0-0 transition (at 600 nm) is associated with the formation of intrachain electronic states, whereas the 0-1 and 0-2 (at 551 and 526 nm, respectively) are due to

interchain excitons.[48] The intensity of the aforementioned transitions varies among functionalized-RGO@P3HT blends, as it can be observed in detail from the inset in Figure 2a. UV-Visible absorption features of P3HT have been widely studied by Spano and coworkers,[49] demonstrating that the coupling between chains during an electronic transition decreases as the polymer chains assume a more extended conjugation length. The degree of coupling can be calculated from the intensity ratio between the lowest energy peak ($I_{0\text{-}0}$) and the first interchain transition ($I_{0\text{-}1}$). In particular, an increase in the $I_{0\text{-}0}/I_{0\text{-}1}$ ratio corresponds to a decrease in the excitonic coupling, hence, an increase in the conjugation length and intrachain order.[50] Since the spectra are normalized at the 0-1 transition, the $I_{0\text{-}0}/I_{0\text{-}1}$ ratios correspond to the normalized intensity of the 0-0 shoulders. As shown in Table 2, the $I_{0\text{-}0}/I_{0\text{-}1}$ intensity ratio for all composites is higher than for P3HT, but there is no correlation with the wt% content of functionalized-RGO, suggesting that differences in the structure of the grafted functionalities affect the absorption features more than the variations in the RGO content of our blends. Indeed, RGO-PhTh@P3HT has the highest $I_{0\text{-}0}/I_{0\text{-}1}$ ratio (that should correspond to the highest degree of planarization of polymer chains) among all blends, while containing the lowest quantity of dispersed RGO derivative. A correlation between $I_{0\text{-}0}/I_{0\text{-}1}$ ratios and FDs of the functionalized-RGO does not result too: the most functionalized derivative is RGO-PhOHex, which furnishes anyway the lowest variation in $I_{0\text{-}0}/I_{0\text{-}1}$ ratio.

**Table 2.** Summary of the UV-vis absorption data for spin-coated films of the five functionalized-RGO@P3HT blends and of bare P3HT

| | | 0-2 | | 0-1 | 0-0 | |
|---|---|---|---|---|---|---|
| **Functionalized-RGO@P3HT blend** | **wt% in P3HT** | **λ (nm)** | **Abs** | **λ (nm)** | **λ (nm)** | **Abs** |
| **P3HT** | - | 526 | 0.99 | 551 | 600 | 0.71 |
| **RGO-PhTh@P3HT** | 5.1 | 533 | 0.95 | 556 | 603 | 0.80 |
| **RGO-PhMeTh@P3HT** | 6.2 | 532 | 0.96 | 556 | 602 | 0.79 |
| **RGO-PhBiTh@P3HT** | 6.7 | 530 | 0.97 | 557 | 601 | 0.78 |
| **RGO-PhOHex@P3HT** | 6.3 | 528 | 0.98 | 554 | 600 | 0.75 |
| **RGO-PhOEtHex@P3HT** | 5.5 | 532 | 0.96 | 556 | 602 | 0.78 |

The red shift of the absorption peaks is also an important proof of the planarity enhancement in the polymer chains. In fact, the higher is the planar fraction of the chains, the higher is the conjugation length and, consequently, the lower is the energy gap between the levels involved in the electronic transition.[49] Focusing on the wavelength values, it is also possible in some cases to track a red shift of the 0-0 peaks that follows the same trend of the $I_{0\text{-}0}$ enhancement, pointing out at different enhancements in the polymer chains planarity induced by the five types of functionalized-RGO materials. The red-shift is indeed clear only in the spectra of those composites in which the $I_{0\text{-}0}$

enhancement is more pronounced, such as RGO-PhTh@P3HT, RGO-PhMeTh@P3HT and RGO-PhOEtHex@P3HT. On the other hand, by looking at the 0-2 transition, a decrease of $I_{0-2}$ is observed in all composites with respect to P3HT, with the highest difference for the RGO-PhTh@P3HT blend and the lower for RGO-PhOHex@P3HT. The interchain 0-2 transition is correlated to the distance between the chains: if the chains are more far apart the probability of an interchain transition decreases and then also $I_{0-2}$ would decrease.[50] Accordingly, RGO-PhTh@P3HT should be the material characterized by the weakest polymer interchain interactions. Among all blends, the $I_{0-2}$ decrease follows an order analogous to that seen for the $I_{0-0}$ enhancement, confirming that the structure of the organic group attached to RGO affects the extent of all together the alterations observed in the polymer absorption spectrum.

Finally, the broad absorption band characteristic of RGO, which is observed in solution (see Figure S6 in the S.I.), is not detectable from the thin-films absorption spectra, likely because of the relatively low filler loadings. However, by looking at the NIR region absorbance of the blends it is possible to notice that this last one is not zero as for neat P3HT, which might be correlated to the existence of scattering RGO species. The presence of the carbon nanofillers in the two blends containing the highest wt% of functionalized-RGO, namely RGO-PhOHex@P3HT (6.3 wt%) and RGO-PhBiTh@P3HT (6.7 wt%), is further inferred through Raman analysis. The spectra reported in Figure 2b show, together with the typical bands associated to P3HT at 1445 $cm^{-1}$ (most intense resonance, due to the in phase stretching vibration of all the C-C double bonds present in the polymer [51]) and 1380 $cm^{-1}$ (of significantly lower intensity and due to the C-C single bonds stretching vibration [51]), the clear appearance of one further signal at 1580 $cm^{-1}$, ascribable to the G band of the two functionalized RGO materials (the Raman spectra of these last ones, featuring both G and D bands, are reported in the inset for the sake of clarity). The thin-films of the five types of functionalized-RGO@P3HT blends were also subjected to steady-state and time-resolved photoluminescence (SS-PL and TR-PL) analyses, revealing insignificant differences with respect to plain P3HT, in both band shapes and PL lifetimes (the corresponding spectra are reported in the S.I., Figure S7 and S8 and the corresponding lifetimes analysis in Table S1).

In an attempt to gain insights into the thin film morphologies of the functionalized-RGO@P3HT blends in comparison to that of bare P3HT, the same samples used for optical analysis were subjected to grazing-incidence X-ray diffraction (GIXRD) analysis. The only signal present in the X-ray diffraction patterns (see Figure S9 in the S.I.) is the one associated with the presence of the polymer crystalline domains at $2\theta = 5.5°$, indexed as 100, proving that the P3HT lamellae in the film adopt an edge-on orientation, where the hexyl-side chains are perpendicular to the glass substrate.[52] The P3HT chains normally lay in this particular orientation, instead of a face-on orientation, when silicon

or weakly interacting substrates are used.[53] The RGO diffraction peak at 2θ = 25° [54] is not visible since its quantity in the blends is too low. From GIXRD data (see S.I. for the detailed analysis, furnishing P3HT interchain distances and sizes of the crystalline domains), a morphological picture illustrating an exclusive localization of the functionalized-RGO fillers within the amorphous region of semicrystalline P3HT films appears as the most reliable one.[55]

The two functionalized-RGO@P3HT blends per type of RGO functionalization (*i.e.* the thienyl-type and the alkyl-type) containing the highest wt% of dispersed CNSs, namely the RGO-PhBiTh@P3HT and the RGO-PhOHex@P3HT blends, were selected to be tested as HTMs in direct architecture PSCs. As already pointed out in the introduction, their performance was compared with that of bare P3HT and of the benchmark Spiro-OMeTAD HTM. Whereas this last one was subjected to a standard doping treatment with 4-*tert*-butylpyridine (TBP) and bis(trifluoromethane)sulfonimide lithium salt (Li-TFSI) to enhance hole mobility,[56] the other three P3HT-based HTMs were used as produced (being dissolved in chlorobenzene, no risks of altering the underlying perovskite layer morphology existed because of solvent orthogonality). In order to evaluate the reproducibility of the solar cells fabrication process, a set of devices for each type of HTM was prepared and characterized. PSCs were based on FTO as the transparent electrode, $C_{60}$ as the electron transporting layer, the perovskite photo-active layer (a mixed cation perovskite active layer with formula $Cs_{0.15}FA_{0.85}PbI_3$ [57, 58]), the HTM and gold as the top metal contact (see Experimental Section for details on device preparation). Our choice of using $C_{60}$ as an ETL is supported by a few reports in the literature which express superior electron transporting properties, ability of passivating interface trap states and simplified deposition of $C_{60}$ and its derivatives with respect to classical inorganic metal oxide ETLs, such as compact $TiO_2$.[58-60] Moreover, devices employing this last one suffer from UV instability and mismatched electronic properties with the perovskite layer, which reflects in a severe current-voltage hysteresis.[58, 61] The overall statistics on devices performance are reported in Figure 2, where results for all the PSCs figures of merit are given, allowing to discuss the effect of the different HTMs on power conversion efficiency (PCE). Focusing on PCEs (Figure 2a), it is immediately evident the large standard deviation encountered within the dataset related to Spiro-OMeTAD containing PSCs (yellow box), even if these solar cells demonstrate good average PCE (9.4%), with 4 devices reaching the best PCE of 15%. On the contrary, all PSCs containing P3HT-based HTMs feature narrower distributions of PCE values around the mean. This happens particularly for PSCs containing the RGO-PhOHex@P3HT HTM (magenta box), with a standard deviation associated to the average PCE at least four times lower than that resulting from Spiro-OMeTAD containing ones, thus demonstrating a notable uniformity of HTM deposition throughout all the prepared devices. The lack of reproducibility in the Spiro-OMeTAD-based PSCs is generally recognized as due to inhomogeneity

of the HTM doping process, with unpredictable variations in the concentration of the oxidized Spiro-OMeTAD species responsible for charge transport.[62] In addition, for the former, graphene containing, solar cells the average PCE is even slightly higher (9.8%) than for the latter ones (but no devices with PCEs above 11% are present). On the other hand, the second graphene containing HTM, namely RGO-PhBiTh@P3HT, yields devices with the lowest average PCE (8.1%), even surpassed

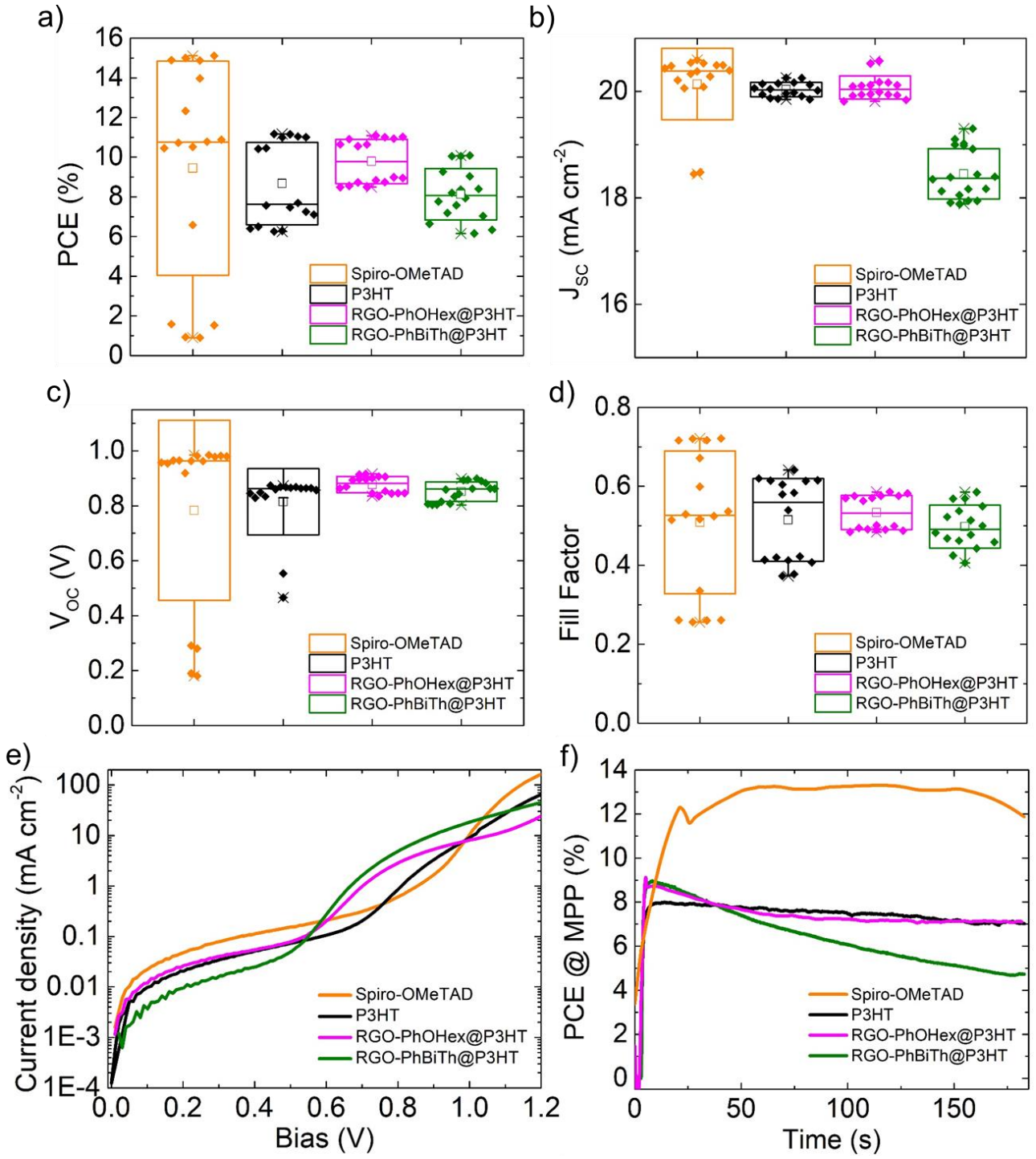


**Figure 2.** Statistical data for figure of merits of PSCs containing the three P3HT-based HTMs and the reference Spiro-OMeTAD HTM: a) power conversion efficiency (PCE), b) short-circuit current density ($J_{SC}$), c) open-circuit voltage

($V_{OC}$) and d) fill factor (FF). Empty squares indicate mean values. e) Dark J-V curves for best devices. f) Stabilized PCE of best devices measured at the maximum power point (PCE@MPP).

by the bare P3HT HTM (8.7%). Open circuit voltage ($V_{OC}$) and fill factor (FF) mean values in PSCs are in a first approximation similar for all the four types of HTMs considered in this work (see Figures2c and 2d), suggesting a good superposition of the different layers within the cells and the presence of little amounts of pinholes. $V_{OC}$ values for P3HT-based devices are perhaps overall slightly lower than for Spiro-OMeTAD-based ones. This is likely due to the intrinsic limitations of P3HT as an HTM, which are thoroughly documented in the literature, such as the higher charge recombination rate and sub-optimal energy level alignment with the perovskite valence band.[41, 63, 64] Indeed, inspection of dark J-V curves of the best devices reported in this work for each of the four considered HTMs (see Figure 2e) show that the built-in voltage ($V_{bi}$) is lower in P3HT-based PSCs with respect to the reference Spiro-OMeTAD device. Also molecular weight of P3HT plays a key role in determining PSC performance,[65] since, as a polymer, P3HT might suffer for difficulties in establishing proper interfacial contact with the perovskite layer, differently from a small molecule such as Spiro-OMeTAD. Nevertheless, it has been also thoroughly demonstrated that, after proper optimization, devices based on P3HT can perform similarly or even better than devices based on Spiro-OMeTAD, while at the same time also employing a material which is readily available at lower costs.[41, 65] On the other hand, short circuit current densities ($J_{SC}$) are extremely variable from case to case (Figure 2b) and are therefore largely responsible for determining the final device performance. From these datasets it emerges clearly the lower contribution in current (10% less) extracted from PSCs containing the RGO-PhBiTh@P3HT HTM with respect to those extracted from the other three types of PSCs. This phenomenon might be related to a higher charge recombination at the perovskite/RGO-PhBiTh@P3HT interface, which could take place, for example, if the carbon nanomaterial contributes to generate internal short-circuits,[66] following local variations of the layer thickness and/or morphology.

Analysis of J-V curves in both forward and reverse scans of the best devices for each HTM (reported in Figure S10 in the S.I.) are not indicative of the real behavior of each HTM and cannot provide a clear estimation of the extent of charge recombination. In this regard, statistical data are the one which should be considered the most (Figure 2), since they regard a full population of devices and not one single, even if the best, case. The existence of a pronounced hysteretic behavior for all HTMs examined is clearly evident from Figure S10. This affects our ability of determining the amount of shunt and series resistances in the devices, which might be related somehow to charge recombination. For this reason, we analyzed dark J-V curves (Figure 2e), in which it is clearly evident that $V_{bi}$ for each PSC changes according to the HTM used. In particular, P3HT-based devices have a lower $V_{bi}$

with respect to the Spiro-OMeTAD reference device. In addition, those containing RGO show a further slight diminution of the $V_{bi}$ with respect to bare P3HT, due to doping with RGO, affecting the position of its Fermi level. Overall, by comparing these data with FF statistical analysis (Figure 2d), we can state that there is a combination of series and shunt resistances which is likely higher for RGO-PhBiTh@P3HT based devices (average FF is indeed slightly lower for these last ones), but which also calls for a deeper interface analysis to be proven. Tracking of PCE at the maximum power-point (PCE@MPP) for the best devices, further highlights the worst performance of RGO-PhBiTh@P3HT based PSCs, showing a steady decrease of PCE over a 180 s period with respect to RGO-PhOHex@P3HT and bare P3HT based ones, for which a constant PCE is recorded along this amount time. Overall, from this scenario emerges RGO-PhOHex@P3HT as the most suitable candidate for replacing the standard Spiro-OMeTAD HTM, due to reproducible and stabilized figures of merit at lower costs of production.

Aiming at understanding the physical reasons behind the decrease in $J_{SC}$ found when employing in PSCs the RGO-PhBiTh@P3HT HTM with respect to the other three tested HTMs, the ability of the four materials to efficiently extract holes from the perovskite layer was evaluated through TR-PL analysis. For this purpose, perovskite samples on glass slides were prepared, on top of which the four different HTMs were deposited following the same procedure used for PSC fabrication (see the Experimental Section for details). Figure 3b reports the TR-PL plots of the four samples, in which the perovskite PL decay has been probed in the range between 800 and 850 nm (the SS-PL spectra of the same samples are given in the S.I., Figure S11). The plain perovskite TR-PL plot is not reported in the same graph, due to the different time resolution window in which its PL decay takes place ( > 50 ns), and it is therefore given in a separate graph in Figure 3a for the sake of clarity.

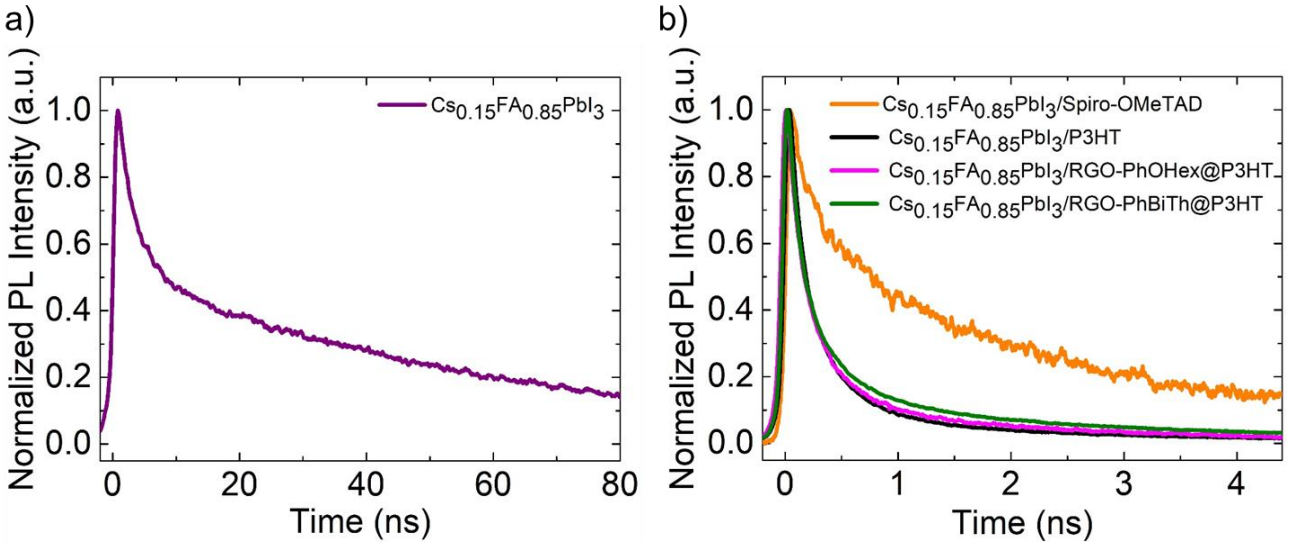


**Figure 3.** TR-PL plots of a) the plain perovskite active layer and b) the perovskite layer with deposited on-top the four different HTMs considered for PSC fabrication, taken between 800 and 850 nm ($\lambda_{exc}$ = 400 nm).

The PL decays are fitted with biexponential (or triexponential) decay function:

$$y(t) = A_1 \exp(t/\tau_1) + A_2 \exp(t/\tau_2) + A_3 \exp(t/\tau_3)$$

where the lifetimes are represented by $\tau_n$ and their corresponding weights are represented by $A_n$. The thus calculated PL lifetimes are reported in Table S3 in the S.I.. From the amount of perovskite PL quenching (all PL lifetimes of the samples containing perovskite/HTM layers are in the range 2-3 ns, thus considerably lower than pristine perovskite PL lifetime), it emerges clearly that the three P3HT-based HTMs are equally efficient in extracting photo-generated charges from the active layer, and perform even better than the standard Spiro-OMeTAD HTM. This excludes a lower hole-extraction ability of the RGO-PhBiTh@P3HT HTM with respect to the others and suggests that the diminished current extracted from the photovoltaic devices containing it might be related to the occurrence of a higher charge recombination at such a perovskite/HTM interface.

In an attempt to further shine light on this aspect, we carried out electrochemical impedance spectroscopy (EIS) analysis on the three types of tested P3HT-based HTMs. Gold coated silicon slides were used as substrates for the three different HTM thin films and the resulting samples were immersed in a 0.1 M $Na_2SO_4$ solution. Nyquist plots for the three different samples are shown in Figure 4a. Experimental data were fitted using a standard equivalent circuit model for a polymer coated metal (Figure 4b).[67] Fitted data reported in Table 4 show that the capacitive coating ($C_c$) is similar for bare P3HT and RGO-PhBiTh@P3HT films, whereas it diminishes 10 times for the RGO-PhOHex@P3HT film. Considering the thickness of the films obtained through profilometric analysis (about 100 nm for bare P3HT, 80 nm for RGO-PhOHex@P3HT and 210 nm for RGO-PhBiTh@P3HT), this result can be linked to a reduced amount of absorbed water onto RGO-PhOHex@P3HT (*i.e.* a diminution of the dielectric constant of the coating, $\varepsilon_r$) with respect to bare P3HT (that has the highest $\varepsilon_r$) and RGO-PhBiTh@P3HT, probably linked to the presence of the hydrophobic hexyl chains covalently bound to the graphene flakes in the former, following the equation:

$$Cc = \frac{\varepsilon_0 \varepsilon_r A}{d}$$

where $\varepsilon_0$is the dielectric constant of vacuum, $A$ is the geometrical area and $d$ the thickness of the coating. More interestingly, the resistance of the pores ($R_P$) is inversely proportional to their area ($A_P$), *i.e.* the active area of the polymer in contact with the electrolyte, according to the equation:[68]

$$R_P = \frac{\rho d}{A_P}$$

where $\rho$ is the conductivity of the solution and $d$ is the thickness of the polymer layer derived from profilometric analysis. Fitted values show that there is a substantial increase of $R_P$ for the RGO-

PhOHex@P3HT film and a slight diminution for the RGO-PhBiTh@P3HT film with respect to bare P3HT, that can be linked to variations of the active area of the film and therefore of the surface roughness. RGO-PhOHex@P3HT appears to be the smoothest one, having an $R_P$ value 30 times bigger than that of P3HT (therefore a smaller $A_P$), whereas RGO-PhBiTh@P3HT is the roughest, having an $A_P$ value that is half that of P3HT. These results can be attributed to the average distribution of the RGO flakes within the P3HT layer: for RGO-PhOHex@P3HT the high value of *Ap* can be correlated to a good uniformity in the dispersion of the nanofillers in the polymer matrix, that notably diminishes the overall surface roughness. On the contrary for RGO-PhBiTh@P3HT, the high roughness can be linked to the presence of graphene clusters on the surface that, in the PSC, might act as recombination sites for holes, thus strongly diminishing the extracted photocurrent.

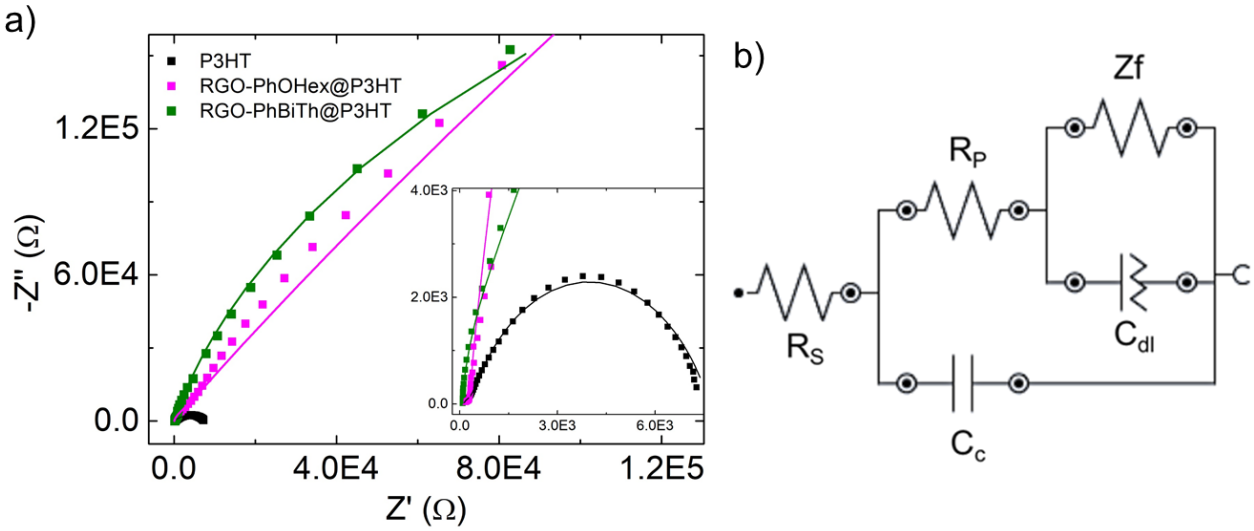


**Figure 4.** EIS characterization of the three P3HT-based HTMs tested in PSCs in this work: a) Nyquist plots (the inset show details at high frequencies) and b) equivalent circuit used for the fitting of experimental impedance data in panel a).

**Table 3.** Fitted data from EIS analysis of the three P3HT-based HTMs tested in PSCs in this work. Percentages indicated in parentheses refer to the error of the fit.

| HTM | $R_s$ (Ohm) | $C_C$ (uF) | N | $R_P$ (kOhm) | Cdl (uF) | N | Z (kOhm) |
|---|---|---|---|---|---|---|---|
| **P3HT** | 122 (2%) | 4.17 (31%) | 0.67 (4%) | 0.3 (9%) | 11.3 (11%) | 0.71 (1.5%) | 7.2 (0.6%) |
| **RGO-PhOHex@P3HT** | 92 (1%) | 0.28 (8%) | 0.97 (1%) | 5.6 (12%) | 2.4 (2.4%) | 0.64 (1%) | 6500 (40%) |
| **RGO-PhBiTh@P3HT** | 168 (2%) | 2.92 (13%) | 0.72 (2%) | 0.17 (5%) | 3.2 (8%) | 0.95 (1%) | 632 (13%) |

This is actually confirmed by looking at the scanning electron microscopy (SEM) images, presented in top view, of the three types of P3HT-based HTMs deposited on top of the perovskite active layer reported in Figure 5. In Figure 5a the perovskite layer is shown, with the characteristic coarse grain morphology, whereas in Figure 5b the photoactive layer covered with the bare P3HT HTM, from

which the grain structure is still notable, even if blurred by the excess surface electrical charging of the sample. Figure 5c and 5d illustrate the cases of the perovskite layer covered with the RGO-PhOHex@P3HT and with the RGO-PhBiTh@P3HT HTMs, respectively. From these images it is evident the most corrugated nature of the carbon-based nanofillers contained in the latter sample with respect to the flatter arrangement of those within the former. The presence of the hexyl chain substituents decorating RGO-PhOHex allows these fillers to film homogeneously with the polymer

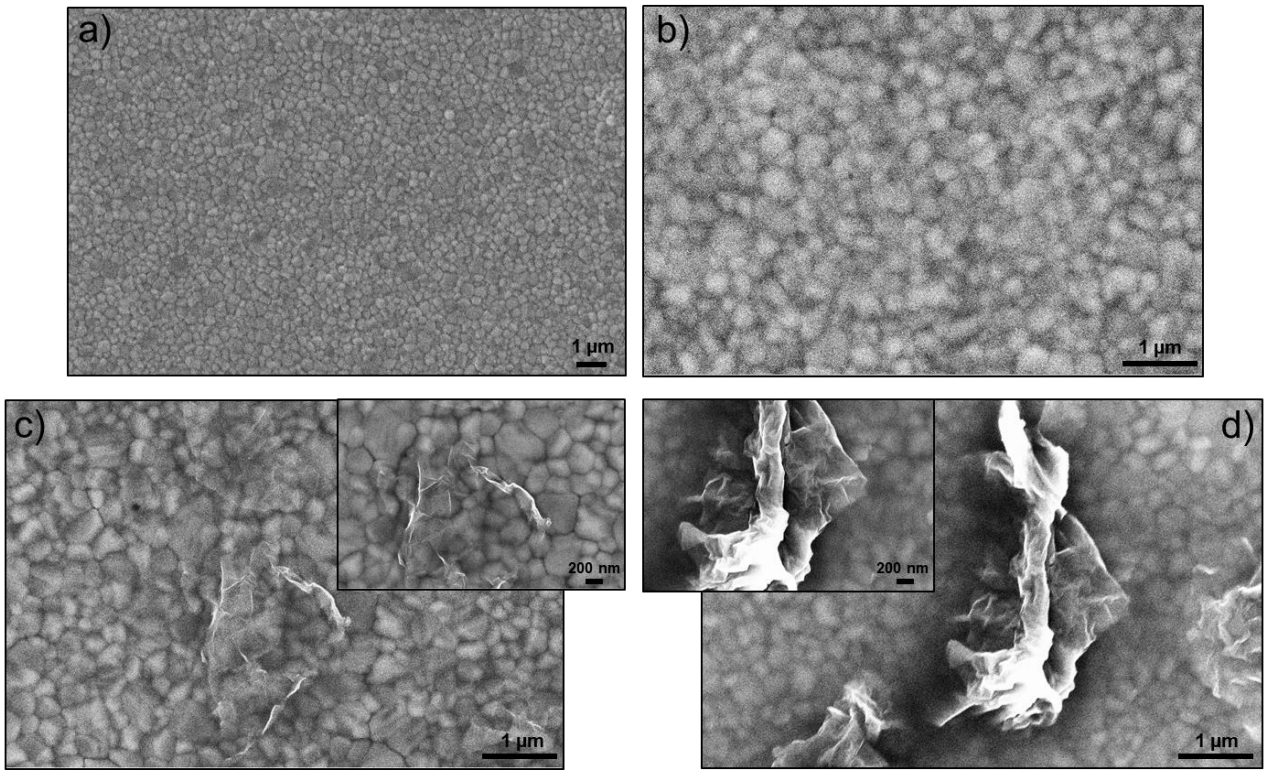


**Figure 5.** Top-view SEM images of a) the plain perovskite active layer and the perovskite layer with deposited on top b) the bare P3HT HTM, c) the RGO-PhOHex@P3HT HTM and d) the RGO-PhBiTh@P3HT HTM. In panels c) and d) details of the RGO flakes contained within the upper layer are given.

layer itself during deposition, yielding little amounts of protrusions escaping from the HTM surface. In addition, from Figure 5c the perovskite layer underneath the HTM is very clearly visible, particularly in the area where the RGO-PhOHex flake is located, indicating that the upper layer is well- conductive. The opposite behavior is instead demonstrated by the RGO-PhBiTh fillers, in which the bithienyl groups bound to the surface are likely responsible for inducing the corrugation of the single flakes, through formation of intramolecular π-stacking interactions. This finally leads to an HTM constituted of a P3HT thin layer from which the self-aggregated RGO flakes protrude significantly, thus contributing in generating short-circuits between the photoactive layer and the top metal electrode that ultimately lower $J_{SC}$ in the photovoltaic device.

Atomic force microscopy (AFM) and scanning Kelvin probe microscopy (SKPM) analysis further confirm the scenario revealed through SEM. Figure S12 in the S.I. shows typical AFM images,

representative of the whole surface of P3HT films embedding RGO-PhOHex and RGO-PhBiTh fillers, in panels S12a and S12d, respectively. Same as for the SEM, but here with direct 3D mapping, topographic AFM images confirm the higher roughness of the RGO-PhBiTh@P3HT.On average, the root mean square (RMS) roughness of these 30×30 $\mu m^2$ areas turns out to be 28 ± 17 nm for RGO-PhOHex@P3HT and 150 ± 90 nm for RGO-PhBiTh@P3HT films, respectively (N=6), with statistically significant difference ($p < 0.01$). The cross sections on the right hand sides (Figures S12c, S12f) confirm this picture visually with profiles (in red) taken across the tallest features in the respective 2D images: RGO-PhBiTh@P3HT is indeed characterized by protrusions reaching almost 1 μm height, while those in RGO-PhOHex do not overpass 150 nm. In panels S12b and S12e (as well in the blue cross-section profiles of 6c and 6f) the SKPM maps of work function, measured simultaneously on the same areas, are also shown. Whereas the mean work function does not change significantly, overall it can be said that the rougher topography affects consequently also the spread in electrical properties of the composite surface, especially at the edges of the features. Indeed, the RMS of the work function increases in the RGO-PhBiTh@P3HT film with respect to the RGO-PhOHex@P3HT film, from 1.7 ± 0.6 eV to 2.5 ± 0.5 eV.

Finally, in order to rule out a possible influence of the variation in P3HT crystalline domains morphologyon top of the perovskite layer on device performance when going from one P3HT-based HTM to another, we carried out GIXRD investigations on samples analogous to those subjected to SEM analysis. From the GIXRD diffraction patterns reported in Figure S13 in the S.I. it is possible to recognize the presence of the 100 P3HT reflection at 2θ values around 5° in all the three P3HT-containing samples (even if very weak in comparison to the signals due to the underlying perovskite layer). This is the same reflection found when examining the bare polymer and its blends with functionalized-RGO in the form of thin films on glass, indicating an edge-on configuration of the P3HT lamellae with respect to the substrate. The presence of such a signal excludes an influence of variations in the polymer crystallinity on device performance and further confirms that, with such composite HTMs, morphological effects conditioning PSC operation are rather to be found in the conformation assumed by the single RGO fillers.

**3. Conclusions**

In this work we have demonstrated the possibility of tuning the morphology of dispersed RGO flakes in a P3HT thin film by tailoring the intermolecular interactions between the two constituents of the composite. This is achieved through the introduction of properly designed chemical functionalities on the CNS surface by means of covalent chemistry. In addition, a process aimed at dispersing the RGO derivatives in the polymer phase, while eliminating the majority of aggregates, unveils a significant influence of the RGO-grafted moiety, whose structure can either recall the thienyl-based

P3HT backbone or the alkyl-based P3HT lateral chains, on the final filler loading achieved in the composite.

Within this framework, after screening five different types of functionalized-RGO fillers, the two RGO@P3HT blends containing the highest amounts of CNS per type of functionalization (*i.e.* thienyl-type or alkyl-type) have been selected to be tested as HTMs in PSCs, moving from the previous demonstration of a strict correlation between a higher functionalized-RGO content and an improved device performance.[29] Surprisingly, the chemical nature of the functional groups grafted to RGO has revealed to be crucial in driving PSC efficiency. In fact, the P3HT blend HTM containing a functionalized-RGO filler decorated with hexyl chains has shown to be able to outperform in average PCE the other type of composite HTM based on bithienyl-decorated RGO, as well as plain P3HT and standard Spiro-OMeTAD HTMs. The physical reason behind the different electrical behavior encountered when employing one functionalized-RGO with respect to the other have been found in the tendency of the bithienyl-functionalized CNS to self-aggregate, inducing protrusions escaping from the P3HT thin layer that ultimately generate local short-circuits and consequently charge recombination events at the perovskite/HTM interface. Particularly remarkable is the high reproducibility found for the PSCs based on RGO-PhOHex@P3HT HTM. This is indeed a key requirement for planning the fabrication of large area (> 50 $cm^2$) PSCs[39] and will constitute the subject of our future investigations, together with studies of the influence of these functionalized-RGO@P3HT HTM on device stability to environmental factors.[39, 69-72]

At the same time, this work demonstrates the possibility to control the morphology of GBMs dispersed within a polymer layer, by modifying the covalently grafted functionalities. This represents *per se* a step forward in the understanding of structure-property relationships in complex soft functional materials: in fact, while RGO-PhOHex@P3HT thin films appear to be suitable for PSCs applications due to their smooth surface, RGO-PhBiTh@P3HT ones, featuring a number of surface wrinkles, might be employed for applications requiring active species with high surface areas, such as photocatalysis[73] or supercapacitors.[74]

## 4. Experimental

*Materials:* All reagents and solvents were purchased from Sigma-Aldrich and used as received if not otherwise specified. P3HT was purchased from Merck (Mw = 94.100 g mol−1, PD = 1.9, RR = 95.5%). RGO powder was purchased from ACS Material, LLC (product No.: GnP1L-0.5g).

*General procedure for the synthesis of functionalized-RGOs.* RGO (20 mg, 1.66 mmol of C) was ultrasonicated in *N*-cyclohexylpirrolidone (15 mL) with a Misonix 3000 titanium tip sonicator using the following pulse parameters: time on = 3 s, time off = 3 s, power level = 4–6 W, for 10 min. The as-obtained dispersion was then transferred into a flask under nitrogen. One of the five different

aniline derivatives (see S.I. for the synthetic procedures) on a 0.83 mmol scale was then added to the stirring suspension of RGO and the mixture was heated up to 80 °C. After reaching the desired temperature, isopentylnitrite (0.11 mL, 0.83 mmol) was further added and the reaction mixture was left to stir for 4 hours. After cooling down to room temperature, methanol (200 mL) was added and stirring was continued for 15 min. The functionalized-RGO materials was then recovered by filtration (using Fluoropore$^{TM}$ membrane filters, 0.2 μm, Merck Millipore) and further washed with methanol (100 mL). After drying the material on the filter with an IR lamp, the functionalized-RGO was detached and characterized through TGA (see S.I.).

*General procedure for the preparation of functionalized-RGO@P3HT blends.* P3HT was dissolved in chlorobenzene at the 15 mg $mL^{-1}$ concentration by adding the solid polymer to the solvent and stirring the mixture overnight at 70 °C. For the formation of each of the five different blends, 15 mg of the desired functionalized-RGO were dissolved in 10 mL of the P3HT solution and the resulting mixture were ultrasonicated for 10 min (employing the same parameters given above). Elimination of major RGO aggregates was then achieved by centrifuging the suspension at 3000 rpm for 3 min (a MR23i Jouan Thermo Scientific centrifuge with a varying angle rotor -model 11174711/11174720- was employed. 10 mL conical bottom glass Duran centrifuge tubes were used). The residues at the bottom of the vessel were washed in chlorobenzene (10 mL) and chloroform (10 mL) and recovered through centrifugation at each of the two washing steps. They were then dried *in vacuo* and weighted on a precision balance to determine the wt% of functionalized-RGO left blended in the P3HT solution. Thin films of the functionalized-RGO@P3HT blends used for optical and morphological characterization were prepared by spin-coating 100 μL on Corning Cover glass slides at 2000 rpm for 40 s, using a WS-650-23 NPP Laurell Technologies spin coater.

*Characterization of functionalized-RGO@P3HT blends.* UV-visible-NIR spectra of the functionalized-RGO@P3HT blends in thin films were recorded on a Varian Cary 5000 spectrophotometer. Micro-Raman spectra were collected with an Invia Renishaw Raman microspectrometer (50× objective) using the 633 nm line of a He–Ne laser. GIXRD patterns were recorded in the diffraction angular range 2θ 2-40° by a Philips X'Pert PRO diffractometer, equipped with a graphite monochromator on the diffracted beam (incident angle 1°, CuKα radiation).

*Photoluminescence analysis.* SS-PL measurements were carried out by exciting samples with the second harmonic (~ 400nm) of a mode locked Ti-Sapphire laser (Mira 900, Coherent) delivering 150 fs pulses at a repetition rate of 76 MHz in reflection geometry. The excitation beam was spatially limited by an iris and focused onto a spot of approximately 50 μm by a 150 mm focal length lens. The power was adjusted using neutral density filters. SS-PL spectra were collected by a spectrograph with a grating of 30 lines $mm^{-1}$ and further recorded by a Hamamatsu em-CCD camera sensitive in

the visible region. The same pulsed excitation was used for TR-PL measurements but PL decays were instead collected with a Hamamatsu streak camera unit working in Synchroscan mode (time resolution ~2 ps) with a cathode sensitive in the visible region. All spectra were corrected for the response of the instrument using a calibrated lamp.

*PSCs fabrication.* FTO substrates were cleaned in a 1% Hellmanex$^{TM}$ III solution, deionized water (2 times), acetone and isopropanol inside an ultrasonic bath set at the temperature of 55°C. Each cleaning step inside the ultrasonic bath was carried out for 15 min. The substrates were then exposed to $O_2$ plasma for 10 min and afterwards they were immediately brought inside a $N_2$ filled glovebox. All of the following described solution preparation procedures were then further carried out in a $N_2$ filled glove box using anhydrous solvents. A 10 mg mL$^{-1}$ C60 solution in 1,2-dichlorobenzene was stirred for 2 h before the spin coating. A 1.35 M perovskite precursor solution was prepared by mixing 52.6 mg of cesium iodide (99.999%, Alfa Aesar 10992), 622.4 mg of lead iodide (99.9985%, Alfa Aesar 12724) and 197.4 mg of formamidinium iodide (Dyesol 879643-71-7) per 1 ml of DMSO:DMF (3:7) solvent mixture. Perovskite precursor solution was stirred for 3 h at the room temperature before the spin coating. Spiro-OMeTAD (Lumtec LT-S922) solution was prepared by first dissolving 72.3 mg of Spiro-OMeTAD in 1 mL of chlorobenzene and then adding 28.8 µL of TBP and 17.5 µL of a 520 mg mL$^{-1}$ Li-TFSI solution in acetonitrile. Solar cells were then assembled as follows. 80 µL of C60 solution were spin coated on top of clean FTO substrates for 60 s at 2000 rpm (2000 acceleration) and then annealed at 110 °C for 45 min. Substrates were then left to cool down. 150 µL of perovskite precursor solution were spin coated on top of C60 covered FTO substrates with the following spin coating recipe: 10 s at 2000 rpm (2000 acc.) and 30 s at 5000 rpm (5000 acc.). 6 s before the end of the spin coating program, 425 µL of toluene were dripped over the spinning substrate. Substrates were then put on a hotplate at the temperature of 170 °C for 10 min. 70 µL of Spiro OMeTAD solution were spin coated at 4000 rpm (4000 acc.) for 30 s. 100 µl of P3HT solution or functionalized-RGO@P3HT blends were spin coated at 2000 rpm (2000 acc.) for 40 s. Spiro-OMeTAD containing devices were left in a dry box for 12 h to induce doping of the hole transporting layer. Solar cells fabrication was completed by thermal evaporation of gold (60 nm) inside a metal evaporator at the pressure of $1 \cdot 10^{-6}$ mbar. Sample for TR-PL analysis were prepared on glass substrates, first by cleaning them analogously to FTO and then spin-coating the perovskite layers employing the same procedure described for solar cell preparation, using freshly prepared perovskite precursor solution. Spiro-OMeTAD or P3HT-based HTMs were spin coated on top of the perovskite layer, also in the same way as for PSCs fabrication.

*PSCs characterization.* All devices were measured on a solar simulator (Oriel Sol3A, Newport) in dark and light conditions, with an output intensity of 96 mW cm$^{-2}$. The current density-voltage (J-V)

characteristics were measured with a Keithley 2400. No light soaking or pre-biasing was applied before the J-V measurement. Voltage scan speed was set to 50 mV $s^{-1}$. The calculated PCEs were normalized to 1 sun (100 mW $cm^{-2}$) intensity. The illuminated electrode area, defined with a back anodized aluminium mask, was 9.38 $mm^2$.

*EIS analysis.* EIS analysis was performed using a PGSTAT302N potentiostat (Autolab, EcoChemie, The Netherlands) equipped with frequency response analyzer modulus. A saturated calomel electrode (SCE) was used as reference electrode, while the counter electrode was a Pt ring electrode and a 0.1 M $Na_2SO_4$ solution was used as electrolyte. The samples were deposited on a Au coated Si(100) wafer masked with a Teflon tape containing a hole with diameter of 5 mm. The measurements were acquired at open circuit potential (OCP) with a perturbation amplitude of 10 mA and a frequency range between $10^5$ and 0.1 Hz. Stable OCP values were obtained with samples in the dark. The film thickness measurements were performed using KLA-Tencor Alpha-Step IQ Surface Profiler on glass. The lengths scanned were 500 µm with a speed of 50 µm $s^{-1}$ and a rate of sampling of 50 Hz. The reported value is the average of four measurement in different points of the same sample.

*SEM characterization.* An ultra-high vacuum Zeiss Supra 40 with GEMINI column FE-SEM was employed. An electron Energy of 3-5 kV, a distance from the sample around 4 mm and a magnification between 20k and 200k were employed. A high efficiency In – Lens secondary electron detector was used during the images acquisition.

*AFM/SKPM characterization.* AFM/SKPM measurements were done simultaneously during the same session by means of an MFP-3D instrument (Asylum Research, CA, USA). A MESP probe (Bruker, CA, USA) was used, with nominal resonant frequency of 75 kHz and tip diameter of 70 nm, after the ~25 nm coating of CoCr providing the required electrical conductivity. The set elevation height for the second pass – during which the surface potential is measured – was 0 nm. The used tip was calibrated preliminary to the measurements *vs* freshly exfoliated highly oriented pirolitic graphite, which was assumed to hold the work function level of 4.65 eV. Thus, the apparent tip work function was found to be 4.93 eV.

**Acknowledgements**

TG, FL and EM acknowledge financial support from Centro Studi di Economia e Tecnica dell'Energia Giorgio Levi Cases of the University of Padova (project OPERA). EM also acknowledge financial support from the University of Padova with the contract P-DiSC #05BIRD2016-UNIPD. We thank Antonio Rizzo for helpful discussion.

**References**

[1] T. Gatti, N. Vicentini, M. Mba, E. Menna, *Eur. J. Org. Chem.* **2016**, *2016*, 1071.

[2] C.-H. Kim, I. Kymissis, *J. Mater. Chem. C* **2017**, *5*, 4598.

[3] L. Chen, W. Liu, X. Su, S. Xiao, H. Xie, C. Uher, X. Tang, *Synth. Met.* **2017**, *229*, 65.
[4] T. Gatti, E. Menna, M. Meneghetti, M. Maggini, A. Petrozza, F. Lamberti, *Nano Energy* **2017**.
[5] T. Gatti, L. Brambilla, M. Tommasini, F. Villafiorita-Monteleone, C. Botta, V. Sarritzu, A. Mura, G. Bongiovanni, M. D. Zoppo, *J. Phys. Chem. C* **2015**, *119*, 17495.
[6] B. C. Thompson, J. M. J. Fréchet, *Angew. Chem.-Int. Edit.* **2008**, *47*, 58.
[7] J. Roncali, *Acc. Chem. Res.* **2009**, *42*, 1719.
[8] J. M. Salazar-Rios, W. Gomulya, V. Derenskyi, J. Yang, S. Z. Bisri, Z. Chen, A. Facchetti, M. A. Loi, *Adv. Electron. Mater.* **2015**, *1*, 1500074.
[9] W. Gomulya, J. M. Salazar Rios, V. Derenskyi, S. Z. Bisri, S. Jung, M. Fritsch, S. Allard, U. Scherf, M. C. dos Santos, M. A. Loi, *Carbon* **2015**, *84*, 66.
[10] S. K. Samanta, M. Fritsch, U. Scherf, W. Gomulya, S. Z. Bisri, M. A. Loi, *Acc. Chem. Res.* **2014**, *47*, 2446.
[11] A. Liscio, G. P. Veronese, E. Treossi, F. Suriano, F. Rossella, V. Bellani, R. Rizzoli, P. Samori, V. Palermo, *J. Mater. Chem.* **2011**, *21*, 2924.
[12] T. Mosciatti, S. Haar, F. Liscio, A. Ciesielski, E. Orgiu, P. Samorì, *ACS Nano* **2015**, *9*, 2357.
[13] M. El Gemayel, S. Haar, F. Liscio, A. Schlierf, G. Melinte, S. Milita, O. Ersen, A. Ciesielski, V. Palermo, P. Samorì, *Adv. Mater.* **2014**, *26*, 4814.
[14] R. Kroon, D. A. Mengistie, D. Kiefer, J. Hynynen, J. D. Ryan, L. Yu, C. Muller, *Chem. Soc. Rev.* **2016**, *45*, 6147.
[15] B. Dörling, J. D. Ryan, J. D. Craddock, A. Sorrentino, A. E. Basaty, A. Gomez, M. Garriga, E. Pereiro, J. E. Anthony, M. C. Weisenberger, A. R. Goñi, C. Müller, M. Campoy-Quiles, *Adv. Mater.* **2016**, *28*, 2782.
[16] J. Yang, Y. Liu, S. Liu, L. Li, C. Zhang, T. Liu, *Mater. Chem. Front.* **2017**, *1*, 251.
[17] S. K. Yadav, R. Kumar, A. K. Sundramoorthy, R. K. Singh, C. M. Koo, *RSC Adv.* **2016**, *6*, 52945.
[18] N. A. Kumar, H. J. Choi, A. Bund, J.-B. Baek, Y. T. Jeong, *J. Mater. Chem.* **2012**, *22*, 12268.
[19] T. Gatti, G. Girardi, N. Vicentini, R. Brandiele, M. Wirix, C. Durante, E. Menna, *J. Nanosci. Nanotechnol.* **2018**, *18*, 1006.
[20] T. Lei, I. Pochorovski, Z. Bao, *Acc. Chem. Res.* **2017**, *50*, 1096.
[21] Z. Chen, J. W. F. To, C. Wang, Z. Lu, N. Liu, A. Chortos, L. Pan, F. Wei, Y. Cui, Z. Bao, *Adv. Energy Mater.* **2014**, *4*, 1400207.
[22] I. Shown, A. Ganguly, L.-C. Chen, K.-H. Chen, *Energy Sci. Eng.* **2015**, *3*, 2.
[23] K. K. H. De Silva, H. H. Huang, R. K. Joshi, M. Yoshimura, *Carbon* **2017**, *119*, 190.
[24] S. Stankovich, D. A. Dikin, R. D. Piner, K. A. Kohlhaas, A. Kleinhammes, Y. Jia, Y. Wu, S. T. Nguyen, R. S. Ruoff, *Carbon* **2007**, *45*, 1558.
[25] T. Gatti, N. Manfredi, C. Boldrini, F. Lamberti, A. Abbotto, E. Menna, *Carbon* **2017**, *115*, 746.
[26] L. Gabrielli, G. Altoè, M. Glaeske, S. Juergensen, S. Reich, A. Setaro, E. Menna, F. Mancin, T. Gatti, *Phys. Status Solidi B* **2017**, *254*, 1700281.
[27] F. Lamberti, L. Brigo, M. Favaro, C. Luni, A. Zoso, M. Cattelan, S. Agnoli, G. Brusatin, G. Granozzi, M. Giomo, N. Elvassore, *ACS Appl. Mater. Interfaces* **2014**, *6*, 22769.
[28] H.-W. Cho, W.-P. Liao, W.-H. Lin, M. Yoshimura, J.-J. Wu, *J. Power Sources* **2015**, *293*, 246.
[29] T. Gatti, S. Casaluci, M. Prato, M. Salerno, F. Di Stasio, A. Ansaldo, E. Menna, A. Di Carlo, F. Bonaccorso, *Adv. Funct. Mater.* **2016**, *26*, 7443.
[30] R. Hu, L. Chu, J. Zhang, X. a. Li, W. Huang, *J. Power Sources* **2017**, *361*, 259.
[31] G. M. Viskadouros, M. M. Stylianakis, E. Kymakis, E. Stratakis, *ACS Appl. Mater. Interfaces* **2014**, *6*, 388.
[32] T. Xie, G. Xie, Y. Zhou, J. Huang, M. Wu, Y. Jiang, H. Tai, *Chem. Phys. Lett.* **2014**, *614*, 275.
[33] N. Boulanger, V. Yu, M. Hilke, M. F. Toney, D. R. Barbero, *Phys. Chem. Chem. Phys.* **2017**, *19*, 8496.
[34] P. Salice, C. Sartorio, A. Burlini, R. Improta, B. Pignataro, E. Menna, *J. Mater. Chem. C* **2015**, *3*, 303.
[35] P. Salice, E. Fabris, C. Sartorio, D. Fenaroli, V. Figà, M. P. Casaletto, S. Cataldo, B. Pignataro, E. Menna, *Carbon* **2014**, *74*, 73.
[36] P. Guarracino, T. Gatti, N. Canever, M. Abdu-Aguye, M. A. Loi, E. Menna, L. Franco, *Phys. Chem. Chem. Phys.* **2017**, *19*, 27716.
[37] J. R. Lomeda, C. D. Doyle, D. V. Kosynkin, W.-F. Hwang, J. M. Tour, *J. Am. Chem. Soc.* **2008**, *130*, 16201.
[38] N. Vicentini, T. Gatti, P. Salice, G. Scapin, C. Marega, F. Filippini, E. Menna, *Carbon* **2015**, *95*, 725.

[39] A. L. Palma, L. Cinà, S. Pescetelli, A. Agresti, M. Raggio, R. Paolesse, F. Bonaccorso, A. Di Carlo, *Nano Energy* **2016**, *22*, 349.
[40] Z. Hawash, L. K. Ono, Y. Qi, *Adv. Mater. Interf.* **2017**, 1700623.
[41] F. Di Giacomo, S. Razza, F. Matteocci, A. D'Epifanio, S. Licoccia, T. M. Brown, A. Di Carlo, *J. Power Sources* **2014**, *251*, 152.
[42] D. Wang, M. Wright, N. K. Elumalai, A. Uddin, *Sol. Energy Mater. Sol. Cells* **2016**, *147*, 255.
[43] W. Zhou, Z. Wen, P. Gao, *Adv. Energy Mater.*, 1702512.
[44] J. L. Bahr, J. M. Tour, *Chem. Mater.* **2001**, *13*, 3823.
[45] M. D'Este, M. De Nardi, E. Menna, *Eur. J. Org. Chem.* **2006**, *2006*, 2517.
[46] Y. Lin, M. J. Meziani, Y.-P. Sun, *J. Mater. Chem.* **2007**, *17*, 1143.
[47] F. Bonaccorso, A. Bartolotta, J. N. Coleman, C. Backes, *Adv. Mater.* **2016**, *28*, 6136.
[48] P. J. Brown, D. S. Thomas, A. Köhler, J. S. Wilson, J.-S. Kim, C. M. Ramsdale, H. Sirringhaus, R. H. Friend, *Phys. Rev. B* **2003**, *67*, 064203.
[49] F. C. Spano, *Chem. Phys.* **2006**, *325*, 22.
[50] J. D. Roehling, I. Arslan, A. J. Moule, *J. Mater. Chem.* **2012**, *22*, 2498.
[51] C. Castiglioni, M. Del Zoppo, G. Zerbi, *J. Raman Spectrosc.* **1993**, *24*, 485.
[52] V. Causin, C. Marega, A. Marigo, L. Valentini, J. M. Kenny, *Macromolecules* **2005**, *38*, 409.
[53] M. Brinkmann, *J. Polym. Sci. Pt. B-Polym. Phys.* **2011**, *49*, 1218.
[54] H. Feng, R. Cheng, X. Zhao, X. Duan, J. Li, *Nat. Commun.* **2013**, *4*, 1539.
[55] P. Kohn, Z. Rong, K. H. Scherer, A. Sepe, M. Sommer, P. Müller-Buschbaum, R. H. Friend, U. Steiner, S. Hüttner, *Macromolecules* **2013**, *46*, 4002.
[56] T. Leijtens, J. Lim, J. Teuscher, T. Park, H. J. Snaith, *Adv. Mater.* **2013**, *25*, 3227.
[57] M. Saliba, T. Matsui, J.-Y. Seo, K. Domanski, J.-P. Correa-Baena, M. K. Nazeeruddin, S. M. Zakeeruddin, W. Tress, A. Abate, A. Hagfeldt, M. Gratzel, *Energy Environ. Sci.* **2016**, *9*, 1989.
[58] P. Topolovsek, F. Lamberti, T. Gatti, A. Cito, J. M. Ball, E. Menna, C. Gadermaier, A. Petrozza, *J. Mater. Chem. A* **2017**, *5*, 11882.
[59] Y. Shao, Z. Xiao, C. Bi, Y. Yuan, J. Huang, *Nat. Commun.* **2014**, *5*, 5784.
[60] Z. Wang, D. P. McMeekin, N. Sakai, S. van Reenen, K. Wojciechowski, J. B. Patel, M. B. Johnston, H. J. Snaith, *Adv. Mater.* **2017**, *29*, 1604186.
[61] T. Leijtens, G. E. Eperon, S. Pathak, A. Abate, M. M. Lee, H. J. Snaith, *Nat. Commun.* **2013**, *4*, 2885.
[62] W. H. Nguyen, C. D. Bailie, E. L. Unger, M. D. McGehee, *J. Am. Chem. Soc.* **2014**, *136*, 10996.
[63] D. Bi, L. Yang, G. Boschloo, A. Hagfeldt, E. M. J. Johansson, *J. Phys. Chem. Lett.* **2013**, *4*, 1532.
[64] Y. Guo, C. Liu, K. Inoue, K. Harano, H. Tanaka, E. Nakamura, *J. Mater. Chem. A* **2014**, *2*, 13827.
[65] N. Y. Nia, F. Matteocci, L. Cina, A. Di Carlo, *ChemSusChem* **2017**, *10*, 3854.
[66] S. Cataldo, P. Salice, E. Menna, B. Pignataro, *Energy Environ. Sci.* **2012**, *5*, 5919.
[67] A. Amirudin, D. Thieny, *Prog. Org. Coat.* **1995**, *26*, 1.
[68] F. Mansfeld, *J. Appl. Crystallogr.* **1995**, *25*, 187.
[69] H. Chen, Y. Hou, C. E. Halbig, S. Chen, H. Zhang, N. Li, F. Guo, X. Tang, N. Gasparini, I. Levchuk, S. Kahmann, C. O. Ramirez Quiroz, A. Osvet, S. Eigler, C. J. Brabec, *J. Mater. Chem. A* **2016**, *4*, 11604.
[70] N. Arora, M. I. Dar, A. Hinderhofer, N. Pellet, F. Schreiber, S. M. Zakeeruddin, M. Grätzel, *Science* **2017**.
[71] A. Agresti, S. Pescetelli, B. Taheri, A. E. Del Rio Castillo, L. Cinà, F. Bonaccorso, A. Di Carlo, *ChemSusChem* **2016**, *9*, 2609.
[72] G. Kakavelakis, T. Maksudov, D. Konios, I. Paradisanos, G. Kioseoglou, E. Stratakis, E. Kymakis, *Adv. Energy Mater.* **2017**, *7*, 1602120.
[73] R. Gonçalves, F. C. Moraes, E. C. Pereira, *Carbon* **2016**, *109*, 57.
[74] C.-T. Chien, P. Hiralal, D.-Y. Wang, I. S. Huang, C.-C. Chen, C.-W. Chen, G. A. J. Amaratunga, *Small* **2015**, *11*, 2929.

**The conformation adopted by single reduced graphene oxide flakes dispersed in a P3HT matrix is determined by the type of organic substituents grafted covalently to their surface**. When these composite materials are employed as hole-transporting materials in perovskite solar cells, their morphology determines performance, with smooth ones providing reproducible devices with good power conversion efficiency (PCE) while crumpled ones generating undesired local short circuits that ultimately reduce PCE.

**Keywords.** Perovskite solar cells, reduced graphene oxide, composites, hole transporting materials, interfacial engineering

T. Gatti*, F. Lamberti, P. Topolovsek, M. Abdu-Aguye, R. Sorrentino, L. Perino, M. Salerno, L. Girardi, C. Marega, G. A. Rizzi, M. A. Loi, A. Petrozza, E. Menna*

**Interfacial morphology addresses performance of perovskite solar cells based on composite hole transporting materials of functionalized reduced graphene oxide and P3HT**